21. Le Bihan D, Breton E, Lallemand D, Grenier P, Cabanis E, Laval-Jeantet M (1986) MR imaging of intravoxel incoherent motions: application to diffusion and perfusion in neurological disorders. Radiology 161:401–407
22. Le Bihan D (1991) Molecular diffusion nuclear magnetic resonance imaging. Magn Reson Q 7:1–30
23. Provenzale JM, Mukundan S, Barboriak DP (2006) Diffusion-weighted and perfusion MR imaging for brain tumor characterization and assessment of treatment response. Radiology 239:632–649
24. Delfaut EM, Beltran J, Johnson G, Rousseau J, Marchandise X, Cotten A (1999) Fat suppression in MR imaging: techniques and pitfalls. Radiographics 19:373–382
25. Li S, Sun F, Jin ZY, Xue HD, Li ML (2007) Whole-body diffusion-weighted imaging: technical improvement and preliminary results. J Magn Reson Imaging 26:1139–1144
26. Torabi M, Aquino SL, Harisinghani MG (2004) Current concepts in lymph node imaging. J Nucl Med 45:1509–1518
27. Will O, Purkayastha S, Chan C et al (2006) Diagnostic precision of nanoparticle-enhanced MRI for lymph-node metastases: a meta-analysis. Lancet Oncol 7:52–60
28. Jaffe CC (2006) Measures of response: RECIST, WHO, and new alternatives. J Clin Oncol 24:3245–3251
29. Weber WA (2006) Positron emission tomography as an imaging biomarker. J Clin Oncol 24:3282–3292
30. Hamstra DA, Rehemtulla A, Ross BD (2007) Diffusion magnetic resonance imaging: a biomarker for treatment response in oncology. J Clin Oncol 25:4104–4109
31. Hamstra DA, Chenevert TL, Moffat BA et al (2005) Evaluation of the functional diffusion map as an early biomarker of time-to-progression and overall survival in high-grade glioma. Proc Natl Acad Sci USA 102:16759–16764
32. Moffat BA, Chenevert TL, Lawrence TS et al (2005) Functional diffusion map: a noninvasive MRI biomarker for early stratification of clinical brain tumor response. Proc Natl Acad Sci USA 102:5524–5529
33. Lee KC, Bradley DA, Hussain M et al (2007) A feasibility study evaluating the functional diffusion map as a predictive imaging biomarker for detection of treatment response in a patient with metastatic prostate cancer to the bone. Neoplasia 9:1003–1011
34. Rohren EM, Turkington TG, Coleman RE (2004) Clinical applications of PET in oncology. Radiology 231:305–332
35. Ichikawa T, Erturk SM, Motosugi U et al (2006) High-B-value diffusion-weighted MRI in colorectal cancer. AJR Am J Roentgenol 187:181–184
36. Ichikawa T, Erturk SM, Motosugi U et al (2007) High-b value diffusion-weighted MRI for detecting pancreatic adenocarcinoma: preliminary results. AJR Am J Roentgenol 188:409–414
37. Tsushima Y, Takano A, Taketomi-Takahashi A, Endo K (2007) Body diffusion-weighted MR imaging using high b-value for malignant tumor screening: usefulness and necessity of referring to T2-weighted images and creating fusion images. Acad Radiol 14:643–650
38. Komori T, Narabayashi I, Matsumura K et al (2007) 2-[Fluorine-18]-fluoro-2-deoxy-D-glucose positron emission tomography/computed tomography versus whole-body diffusion-weighted MRI for detection of malignant lesions: initial experience. Ann Nucl Med 21:209–215
39. Tamai K, Koyama T, Saga T et al (2007) Diffusion-weighted MR imaging of uterine endometrial cancer. J Magn Reson Imaging 26:682–687
40. Tamai K, Koyama T, Saga T et al (2007) The utility of diffusion-weighted MR imaging for differentiating uterine sarcomas from benign leiomyomas. Eur Radiol DOI 10.1007/s00330-007-0787-7
41. Stadnik TW, Demaerel P, Luypaert RR et al (2003) Imaging tutorial: differential diagnosis of bright lesions on diffusion-weighted MR images. Radiographics 23:e7
42. Muro I, Takahara T, Horie T et al (2005) Influence of respiratory motion in body diffusion weighted imaging under free breathing (examination of a moving phantom). Nippon Hoshasen Gijutsu Gakkai Zasshi 61:1551–1558
43. Nasu K, Kuroki Y, Sekiguchi R, Nawano S (2006) The effect of simultaneous use of respiratory triggering in diffusion-weighted imaging of the liver. Magn Reson Med Sci 5:129–136
44. Takahara T, Ogino T, Okuaki T et al (2007) Respiratory gated body diffusion weighted imaging avoiding prolongation of scan time: tracking only navigator echo (TRON) technique. Presented at the Joint Annual Meeting ISMRM-ESMRMB, Berlin, Germany, May 19–25, 2007
45. Laghi A, Paolantonio P, Iafrate F, Altomari F, Miglio C, Passariello R (2002) Oral contrast agents for magnetic resonance imaging of the bowel. Top Magn Reson Imaging 13:389–396
46. Kuhl CK, Textor J, Gieseke J et al (2005) Acute and subacute ischemic stroke at high-field-strength (3.0-T) diffusion-weighted MR imaging: intraindividual comparative study. Radiology 234:509–516
47. Murtz P, Krautmacher C, Traber F, Gieseke J, Schield HH, Willinek WA (2007) Diffusion-weighted whole-body MR imaging with background body signal suppression: a feasibility study at 3.0 Tesla. Eur Radiol 17:3031–3037

Magn Reson Med Sci, Vol. 6, No. 4, pp. 211–224, 2007

REVIEW

Practical Aspects of Assessing Tumors Using Clinical Diffusion-weighted Imaging in the Body

Dow-Mu KOH[1]*, Taro TAKAHARA[2,3], Yutaka IMAI[2], and David J COLLINS[1]

[1]*CR UK Clinical Magnetic Resonance Research Group, Institute of Cancer Research and Academic Department of Radiology, Royal Marsden Hospital Downs Road, Sutton SM2 5PT, UK*

[2]*Department of Radiology, Tokai University Hospital, Japan*

[3]*Division of Radiology, Radiotherapy and Nuclear Medicine, University Medical Centre, Utrecht, Netherlands*

(Received July 23, 2007; Accepted September 5, 2007)

Diffusion-weighted magnetic resonance (MR) imaging (DWI) is increasingly applied to evaluate tumors in the abdomen and pelvis. However, DWI is susceptible to a variety of artifacts that arise from motion, use of strong gradient pulses, and echo-planar imaging technique. We discuss practical issues to help radiologists optimize the use of DWI to evaluate tumors in the body, including breath-hold DWI, multiple-acquisition non-breath-hold DWI, and diffusion-weighted whole-body imaging with background body signal suppression (DWIBS). Considerations of meticulous technique, sequence optimization, and quality assurance are emphasized for consistent acquisition of high quality images. We illustrate the potential use of these techniques to detect and characterize tumors and to monitor treatment effects.

Keywords: ***magnetic resonance imaging, diffusion, technique***

Introduction

Diffusion-weighted magnetic resonance imaging (DWI) probes the diffusion of water in the body. The motion of water molecules in the extra- and intracellular spaces and intravascular space contributes to the net water displacement measured by DWI. The technique yields qualitative and quantitative information that reflects tissue cellularity and cell membrane integrity and thus complements morphological information obtained by conventional MR imaging.

Performing DWI in the body is challenging because the inhomogeneity of the magnetic field over a large imaging area and motion arising from different organs conspire to degrade image quality. In the past decade, a series of technological advancements in MR imaging, including higher amplitude gradients, echo-planar imaging (EPI), parallel imaging techniques, and the use of respiratory gating and cardiac triggering for motion compensation, has helped overcome many of these issues. Of these, the development of parallel imaging has been critical because its enables use of very short echo time and reduced echo-train length for very quick acquisition of images with good signal-to-noise that are relatively undegraded by motion and local field gradients.

High quality DWI images can be routinely obtained using modern 1.5T MR imaging systems from the major manufacturers (e.g., General Electric, Milwaukee, USA; Siemens, Erlangen, Germany; Philips, Eindhoven, The Netherlands). However, implementation of DWI sequences differs among manufacturers, and the reader should be familiar with the strengths and limitations of their own imaging systems to optimize imaging performance. In this regard, the radiologist should work closely with the physicist and technologist in establishing scanning protocols to ensure acquisition of images of consistently high quality.

We discuss the advantages and disadvantages of commonly applied DWI strategies in the body and important considerations for image optimization to ensure high quality images for qualitative visual assessment or quantitative analysis, and we illustrate the potential use of these techniques to detect and

*Corresponding author, Phone: +44-208-661-3340, E-mail: dowmukoh@icr.ac.uk

characterize tumors and to demonstrate treatment response. We assume knowledge of and will not discuss the basic principles of DWI.[1]

DWI Imaging Strategies in the Body

DWI imaging in the body is frequently performed using modified single and dual spin-echo sequences with the application of motion-probing gradients placed on either side of the 180° refocusing pulses. This is combined with echo-planar imaging (EPI) readout and parallel acquisition techniques (e.g. SENSE, GRAPPA) to minimize imaging time, thus preserving image signal-to-noise and reducing motion-related artifacts, without significantly impacting apparent diffusion coefficient (ADC) calculations.[2]

Current widely used imaging strategies for DWI in the body include: (1) breath-hold single-shot DWI, (2) non-breath-hold multiple averaging DWI, and (3) non-breath-hold multiple averaging DWI performed at multiple body stations (diffusion-weighted whole-body imaging with background body signal suppression [DWIBS]). Although each of these strategies is suitable for general imaging of the abdomen and pelvis, the selection of imaging sequence may be influenced by the anatomical region being investigated, whether the images are to be analyzed qualitatively or quantitatively, and the size and heterogeneity of lesions evaluated. Table summarizes typical examples of these imaging approaches.

Breath-hold single-shot DWI. The key advantage of using breath-hold single-shot DWI is the short image acquisition time. For example, the entire liver can be evaluated over 2 breath-holds, each lasting only 20 s. Combining parallel imaging and single-shot EPI measurements allows very short echo times (e.g., 45 to 75 ms), thereby preserving signal-to-noise.[3,4] Furthermore, breath-hold single-shot DWI would be theoretically more effective in characterizing lesion heterogeneity (e.g., on a pixel-by-pixel basis) and in quantifying the ADC of smaller lesions because such information is less likely to be degraded by the volume averaging that occurs with free-breathing techniques.

However, single-shot measurements are inherently noisy because of the low signal-to-noise of the source data. Although artifacts arising from breathing motion are reduced, pulsatile motion from the heart and the aorta can still induce artifacts. Therefore, some advocate combining this technique with cardiac pulse triggering to improve image quality and ADC calculation.[5] However, the use of pulse triggering increases image acquisition time and may render the images more prone to bulk motion. Cardiac pulsation artifacts have been shown to increase ADC measurement in the left lobe of the normal liver compared with the right lobe.[6] The need for good signal-to-noise also means that breath-hold imaging may require thicker slice partitions (6 to 8 mm). Another potential disadvan-

Table. Diffusion-weighted MR imaging sequences for evaluating tumors in the body*

Technique	Breath-hold single-shot echo-planar (EPI) diffusion-weighted imaging (DWI)	Free-breathing multiple averaging single-shot EPI DWI	Whole-body DWI with background suppression
Field of view	340–400 cm	340–400 cm	380–400 cm
Matrix size	112 × 256	112 × 256	160 × 256
Repetition time	2500	3900	> 3500 ms
Echo time	56–68 ms	78	72 ms
Fat suppression	SPAIR	SPAIR/STIR	STIR
EPI factor	65	59	47
Parallel imaging factor	2	2	2
NSA	Single-shot	5	6
Section thickness	7 mm contiguous	5 mm	4 mm/1 mm overlap
Directions of motion-probing gradients	Phase, frequency, and slice	Phase, frequency, and slice	Phase, frequency, and slice
b-factors (s/mm²)	usually 3 b-values (e.g., 0, 100, 500 s/mm²)	allows multiple b-values (e.g., 0, 50, 100, 250, 500, 750 s/mm²)	0 and 1000 s/mm²

* Imaging protocols as implemented on a Philip's 1.5T magnetic resonance imaging system
• STIR = Short-tau inversion recovery
• SPAIR = Spectral selected attenuated inversion recovery

tage of this technique is the number of b-values that can be accommodated within a single breath-hold, which may have bearing on the accuracy of ADC determination.

Free-breathing multiple-averaging DWI. The principle advantages of free-breathing multiple-averaging DWI are that signal averaging allows use of multiple b-values and thin slice partitions (e.g. 4 to 5 mm) and the technique yields images with high signal-to-noise. These images can be qualitatively assessed using multi-planar reconstruction (MPR) or maximum intensity projection (MIP) (Fig. 1).[7] In addition, DWI or ADC maps may be effectively laid over morphological information to produce fusion images that combine diffusion-weighted functional information with anatomical details (Fig. 1). Using multiple b-values also enables evaluation of the ADC of lesions. Thus, free-breathing multiple averaging DWI appears to be a versatile technique that allows good use of DWI images for both qualitative and quantitative analysis.

However, ADC calculation using this technique may be less optimal in characterizing smaller lesions or in reporting lesion heterogeneity because of volume averaging. So, there is considerable interest in combining such sequences with respiratory[8,9] and cardiac triggering techniques to improve image registration and ADC assessment. Not surprisingly, it has been shown that compared with free-breathing acquisition, the use of respiratory triggering in the liver lead to better contrast-to-noise ratio and a decrease in the scattering of ADC values.[8] However, implementing such a scheme in clinical imaging is challenging because it may further increase the already noticeable scan time of 4 to 6 min for each acquisition. Novel techniques that enable more efficient gains in signal acquisition during respiratory gating are being investigated and developed.

Diffusion-weighted whole-body imaging with background body signal suppression (DWIBS). DWIBS was conceived primarily as a method to visualize tumors in the body by their restricted water mobility. Because these images are usually evaluated qualitatively, only b-values of 0 and 1000 s/mm^2 are employed. Fat suppression and high b-value are used to maximize background suppression. Free-breathing multiple averaging DWI is repeated at contiguous imaging stations. The images are processed by MIP, composed together and displayed using an inverted gray scale.[7] The dataset can also be visualized in 3D using MPR and volume rendered (VR) displays (Fig. 2).

Signals from normal tissue, such as blood vessels, fat, muscle and bowel are usually suppressed, whereas other normal structures, such as the spleen, prostate, testes, ovaries, endometrium, and spinal cord, remain visible.[7] DWIBS detects not only tumor (i.e., restricted diffusion) but also hyperviscous fluids (i.e., nonrestricted diffusion with hyperviscosity), such as abscesses. The technique appears promising for detecting tumors of small volume in the lymph nodes, peritoneum, and other sites of occult disease.[7] It can also be used to visualize peripheral nerves as diffusion-weighted MR neurography (Fig. 3).[10]

DWIBS can be obtained using a sophisticated whole-body coil array system, like the total imaging matrix system (TIM, Siemens Medical Solutions, Malvern, Pennsylvania) or other commercially available long coil arrays. However, such imaging can also be achieved using just a single coil array. To do this, the patient lies on a table extension elevated from the MR table-top at the 2 ends by spacers. A 4-cm gap between the table extension and the MR table-top allows the posterior coil elements to be placed under the patient. Placing the posterior coil in this gap enables movement of its element freely to another imaging station without moving the patient or altering the referenced scan position. In this way, images acquired at different imaging stations can be composed to yield a whole-body image (Fig. 4).

DWIBS shares many of the advantages of free-breathing multiple averaging DWI, such as thin image partitions and good signal-to-noise. Its main disadvantage is the relatively long image acquisition time required to evaluate the entire body.

Optimization of DWI in the Body

The image contrast at DWI relies on intrinsic differences in the water diffusion between tissues. To maximize this contrast to detect and characterize lesions, scanning parameters must be chosen that optimize signal and contrast-to-noise between the tumor and surrounding tissues and that minimize artifacts and other effects that may modify or confound the native diffusion-weighted contrast. Appreciation of these factors will help the radiologist make informed decisions at clinical scanning.

Fat suppression. Fat suppression is routinely employed to increase the dynamic range of the DWI images and reduce the chemical shift-induced ghosting that is prevalent in EPI. When performing DWI over a large area of the body, an inversion-recovery (e.g., STIR) approach is preferred because it is likely to produce more uniform fat suppression and is the method adopted for DWIBS. However,

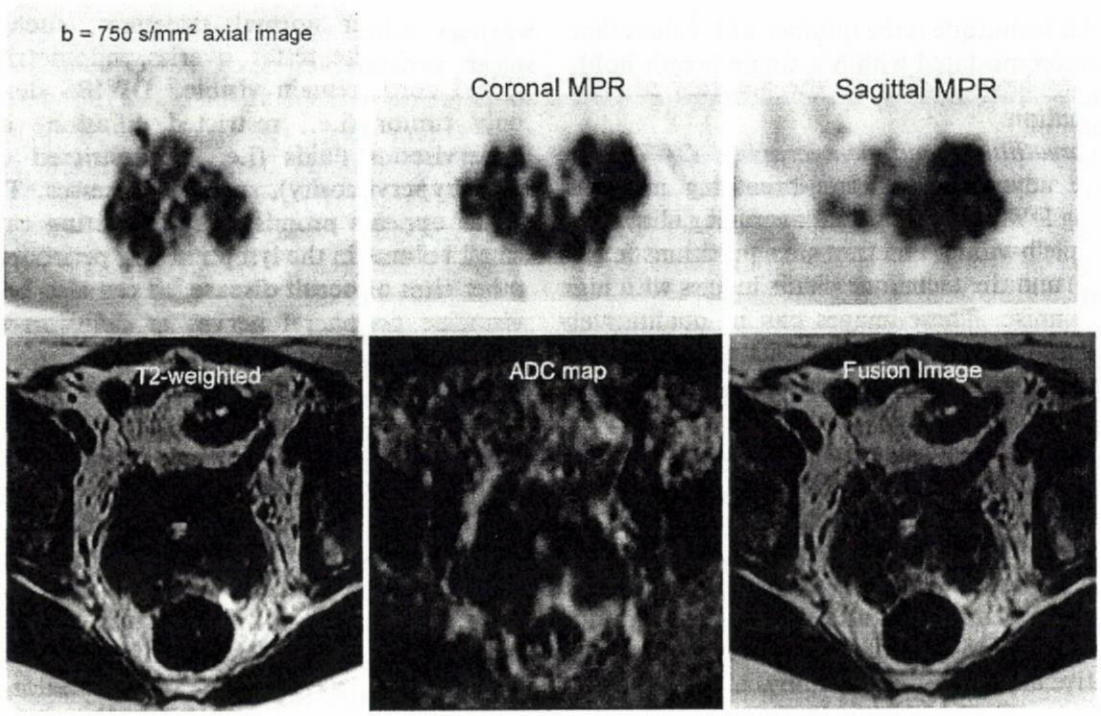

Fig. 1. Free-breathing multiple averaging diffusion-weighted imaging. Study in a 54-year-old woman shows a large mass within the rectouterine pouch that demonstrates restricted diffusion on the b = 750 s/mm² image displayed using an inverted gray scale. Thin image partitions produce images of good signal-to-noise that allow multi-planar reformats. Note the corresponding T_2-weighted image and the apparent diffusion coefficient map. The diffusion-weighted axial image could also be displayed using a color scale (tumor colored red and orange) and fused with the T_2-weighted image to provide combination of functional and anatomical information.

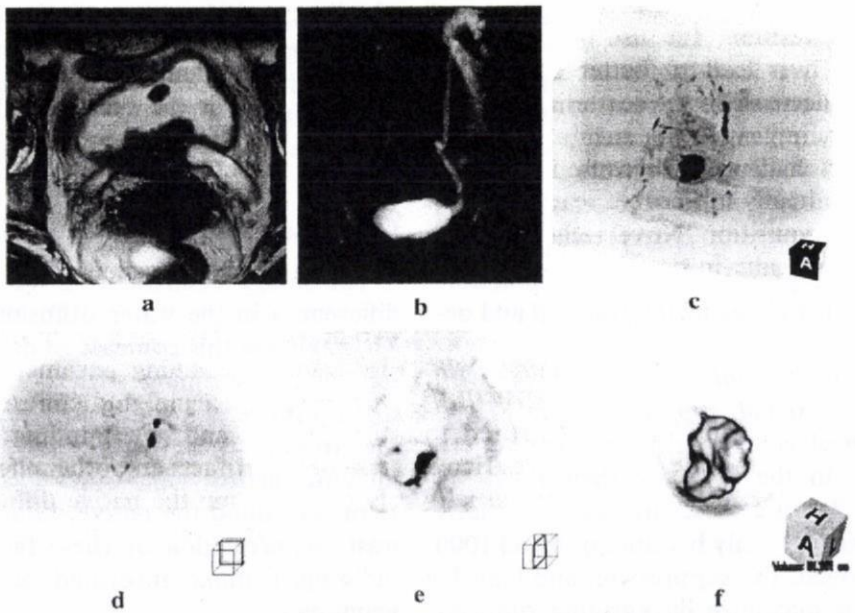

Fig. 2. Three-dimensional displays of diffusion-weighted images with background suppression (DWIBS) technique. A 66-year-old woman with bladder cancer. **(a)** Axial T_2-weighted image shows large bladder cancer in the posterior wall and small daughter nodule anteriorly. **(b)** T_2-weighted magnetic resonance urography shows bilateral hydronephrosis from obstruction of the ureterovesicle junctions. **(c)** Maximum intensity projection of DWIBS image showing main tumor and metastatic left common iliac nodes. **(d)** Axial reformat (8-mm slice thickness, obtained from 4-mm source image) demonstrates metastatic left iliac nodes. **(e)** Sagittal reformat shows main posterior tumor and small anterosuperior daughter nodule. **(f)** Volume rendering image shows 3D shape of the tumor. Images **(c)** to **(f)** are derived from one thin section data set.

in imaging selected areas in the body, such as the liver, chemical fat selective saturation (e.g., spectral selected attenuation with inversion recovery [SPAIR], chemical shift selective [CHESS]) or water-selective excitation may be more useful because these methods produce better signal-to-noise because the repetition time is increased using the STIR technique as the nulling period is of the order of 0.693×300 ms per slice. In addition, using conventional STIR imaging, some of the potential signal is lost by the inversion of all spins, including those associated with water molecules. With SPAIR imaging, only the protons associated with fat are affected by the inversion pulse. One practical step to ensure optimum fat suppression is to perform higher order or advance shimming prior to image acquisition.

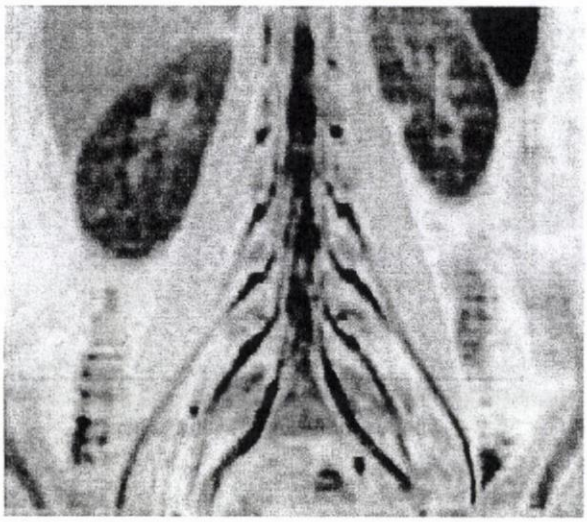

Fig. 3. Diffusion-weighted magnetic resonance neurography. Inverted gray scale maximum intensity projection diffusion-weighted imaging with background suppression image of the lumbar spine of a healthy volunteer showing details of the lumbar plexus.

Minimize T_1 saturation and T_2 shine-through effects. When performing DWI in the body, the repetition time should be sufficiently long to avoid T_1 saturation effects, particularly for the target tissues under evaluation. T_1 saturation can result in spuriously low calculated ADC values. In the liver, for example, malignant lesions such as metastases have a mean T_1 relaxation time of approximately 610 ms.[11] As such, a repetition time of at least 3 times the T_1 relaxation time of the tissue would help to avoid T_1 saturation effects. (N.B. This provides 95% of the longitudinal magnetization recovery. Ideally, a choice of 5 times the T_1 relaxation time of tissue provides 99% magnetization recovery, but this can be impractical, particularly for breath-hold studies). However, even longer repetition times would be required to ensure elimination of this effect in structures with longer T_1 relaxation times (e.g., liver cysts with mean T_1 relaxation time of up to 1 to 2 s).

The other confounding influence on the diffusion-weighted contrast is the T_2 shine-through effect that occurs as a result of high signal intensity

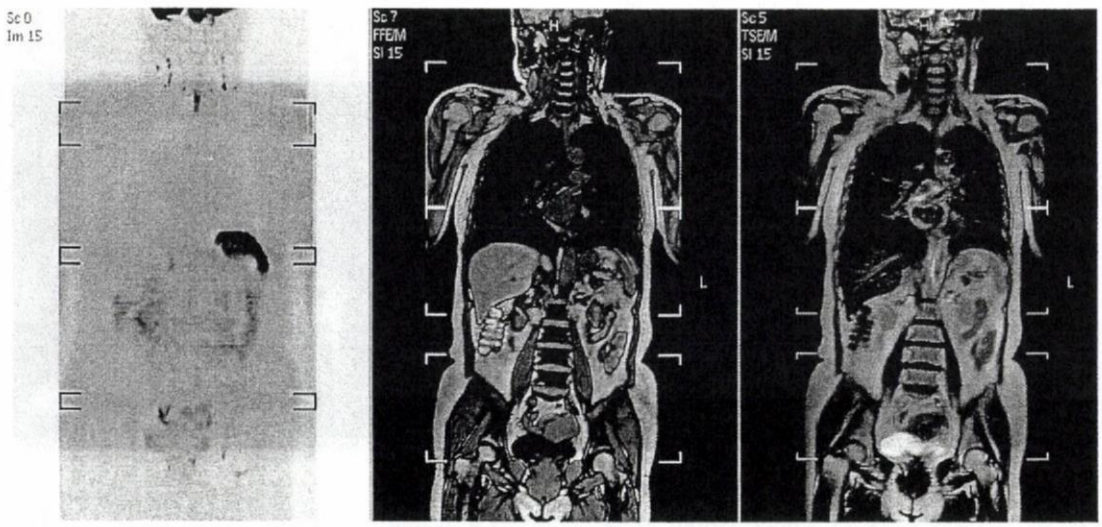

Fig. 4. Example of whole-body diffusion-weighted imaging with background suppression (WB-DWIBS) image obtained from merging 3 image segments acquired using a single coil array. Using the operator console allows merging and display of diffusion- (left), T_1- (middle), and T_2-weighted (right) images from 3 contiguous datasets acquired using the coil sliding technique.

returned from tissues with long intrinsic T_2 relaxation times contributing to the overall measured diffusion-weighted signal. Visual assessment alone may falsely ascribe the high signal intensity observed to restriction in water diffusion. This phenomenon is more difficult to avoid but may be overcome by using an exponential image[12] or calculating the ADC (Fig. 5).

Choice of b-values. When choosing the magnitude and number of b-values to be applied for DWI, considerations should include the DWI technique used, the anticipated image signal-to-noise, the target organ being evaluated, and whether DWI is primarily used for qualitative or quantitative analysis.

When DWI is performed with increasing b-values, the attenuation of the signal intensity in abdominal organs has been shown to be biexponential for the range used for clinical imaging in the body (e.g., b = 0 to 1000 s/mm²). An initial rapid decrease in signal intensity with a small increase in b-value is followed by a more gradual slope of signal attenuation as the b-value increases further. A summary plot derived from published literature values and our own experiments suggests that the initial rapid signal attenuation extends to a b-value of about 100 s/mm² (Fig. 6).

With this in mind, the use of only 2 b-values at DWI[13] will not adequately characterize this biexponential behavior, but it would be possible to derive ADC calculations to reflect this phenomenon using at least 3 b-values. An ADC calculated using only low b-values ($\leq$100 s/mm²; sometimes referred to as ADC*fast* or ADC*low*) will be sensitive to intravoxel capillary perfusion. By contrast, ADC calculations derived from images of b-values greater than 100 s/mm² (sometimes referred to as ADC*slow* or ADC*high*) will be relatively perfusion insensitive and theoretically more reflective of tissue cellularity and the integrity of cellular membranes. Of course, ADC can still be calculated over an entire range of b-values, and such an approach has been established in clinical practice for many

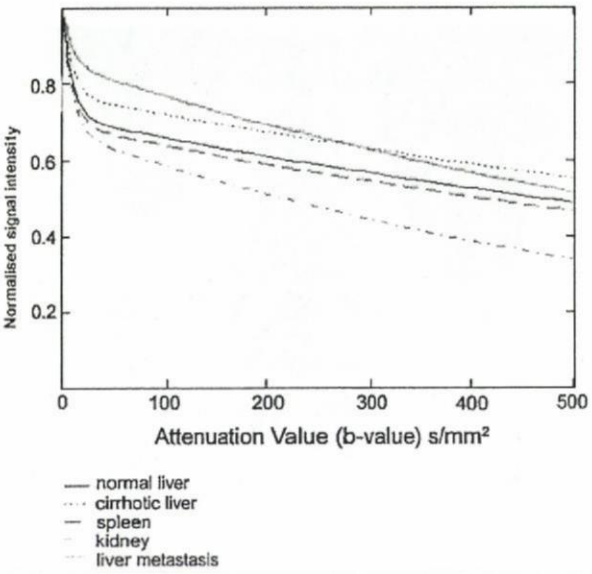

Fig. 6. Signal attenuation in intra-abdominal organs. Graph showing biexponential signal attenuation in major intra-abdominal organs with increasing diffusion weighting. Note the initial rapid signal attenuation with a small increase in b-value, followed by a more gradual slope of signal attenuation beyond approximately b = 100 s/mm².

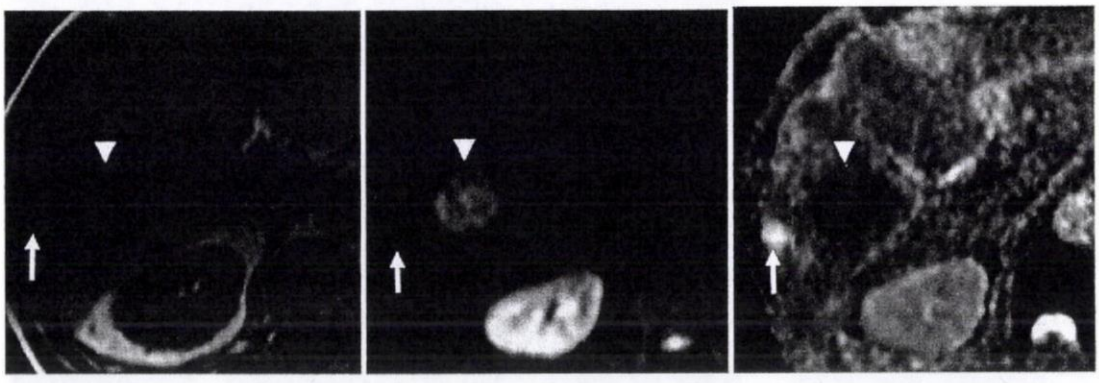

Fig. 5. Overcoming T_2 shine-through using apparent diffusion coefficient (ADC) maps. **(a)** T_1-weighted axial image of the liver showing a small cyst (arrow) and larger metastases (arrowhead). **(b)** At diffusion-weighted imaging, both cyst and metastasis return high signal on b = 500 s/mm² image. **(c)** The ADC map confirms the cyst as showing high ADC (bright) compared with the metastases, which return a low ADC value.

years. Indeed, the intravoxel incoherent motion (IVIM) equation has been applied to characterize the biexponential behavior. However, fractionating the ADC calculations into ADC*fast* and ADC*slow* may potentially be more informative, especially for evaluating treatment response, because drug treatment (e.g., antiangiogenic drug) may reduce blood flow (decrease ADC*fast*) and tissue cellularity (increase ADC*slow*) with little change in overall ADC value. (Fig. 7)

The influence of the choice of b-value on ADC calculations can be observed in the literature. For example, in liver metastases, ADC values calculated using relatively low b-values (e.g., <100 s/mm^2)[14] are higher than ADC calculations obtained using larger b-values (e.g., >100 s/mm^2).[13,15-17] It has also been shown that the mean ADC of colorectal liver metastases calculated over a range of b-values (0, 150, and 500 s/mm^2) is higher than that calculated using higher b-values only (150 and 500 s/mm^2).[18] Similarly, ADC*fast* calculated using low b-values are usually higher than ADC*slow* derived from higher b-values (Fig. 8). More recently, it was shown in normal volunteers that portal perfusion exerted a significant effect when a b-value of 200 s/mm^2 was used, and the ADC measurement of the liver was more reproducible when only higher b-values ($b=500$ and 750 s/mm^2) were employed.[19]

Although it may seem prescriptive to recommend b-values for tumor imaging in the body, DWI for quantifying tumor ADC should include a range of b-values that enables calculation of the ADC*fast* and ADC*slow*. When using non-breath-hold multiple averaging DWI imaging, multiple b-values can be employed to achieve this (e.g., $b=0$, 50 100, 250, 500, 750 s/mm^2). However, when breath-hold imaging is used, there is a limit to the number of b-values that can be accommodated within each breath-hold without increasing the echo or acquisition time. Thus, the choice of 3 appropriate b-values (e.g., $b=0$, 100, 500 s/mm^2) is practical when using breath-hold imaging and still enables the fractionating of the ADCs.

Some authors have employed very low b-values (e.g., $b=3$ s/mm^2) for DWI study.[20] However, ensuring the validity of these small b-values requires proper account of the diffusion weighting introduced by the imaging sequence read-out gradients. Furthermore, some MR systems do not permit the use of very low b-value. Hence, to facilitate meaningful data comparison between centers, it would be useful to ensure that the smallest diffusion weighting applied for imaging can be effectively achieved on other MR systems.

When performing DWIBS, a higher b-value (1000 s/mm^2) is typically used to maximize background signal attenuation and suppression.[7] However, it has to be remembered that the greater signal attenuation at higher b-values usually requires a larger number of signal averages (e.g., $n=4$ to 6) to maintain good signal and contrast-to-noise.

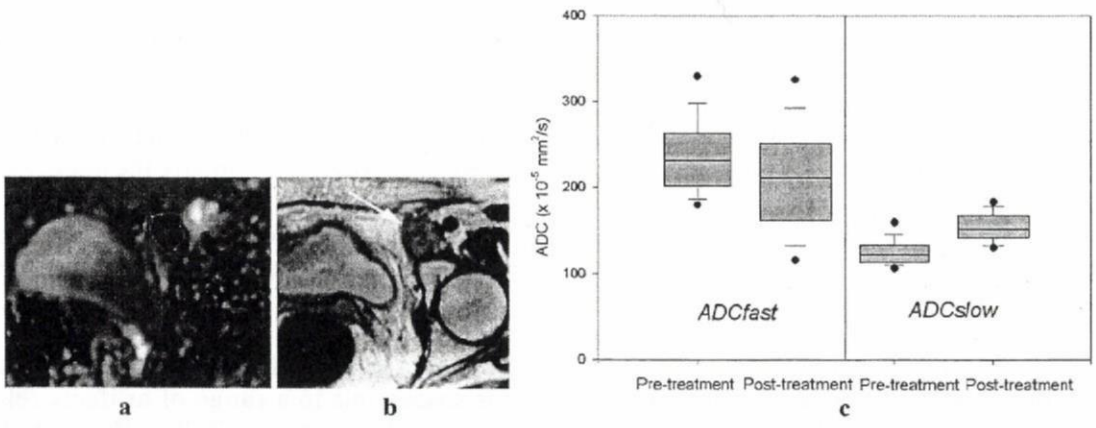

Fig. 7. Evaluating treatment response. Assessment of response made using free-breathing multiple averaging diffusion-weighted imaging, (**a**) apparent diffusion coefficient (ADC)*fast* and (**b**) T_2-weighted image showing an irregular 3-cm left inguinal node (arrow) in a 54-year-old woman with metastatic ovarian cancer. (**c**) Box and Whisker plots of the pixel values of ADC*fast* and ADC*slow* within a region of interest drawn over the lymph node before and at one week after treatment with a novel antivascular drug. Lines through boxes indicate median ADC value, and the whiskers indicate the 5th and 95th percentile values. Rounded circles define the 95% confidence interval. After treatment, there was a significant decrease in the ADC*fast* with a contemporaneous significant increase in the ADC*slow* ($P<0.001$, Wilcoxon signed rank test).

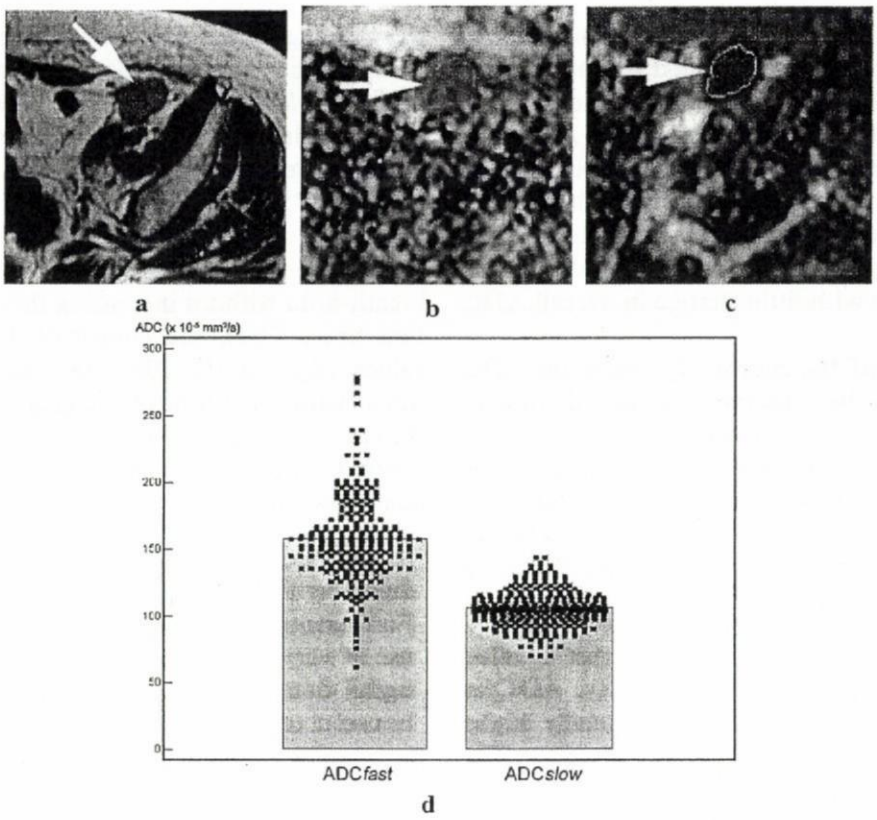

Fig. 8. Apparent diffusion coefficient (ADC)*fast and* ADC*slow*. (**a**) T_2-weighted magnetic resonance imaging showing a 4-cm left external iliac lymph node (arrow). A similar region of interest was drawn encompassing the node (arrows) on the (**b**) ADC*fast* (from b = 0 and 150 s/mm² images) and (**c**) ADC*slow* (from b = 150 and 500 s/mm² images) maps. (**d**) The mean ADC*fast* was higher than the mean ADC*slow* (gray bars). Individual pixel values within the region of interest are plotted as black dots.

Motion-probing gradients. Because water diffusion in tumors and major abdominal organs (except the kidneys) is typically isotropic, it has been suggested that the motion-probing gradient can be applied in just a single direction in abdominal organs showing isotropic diffusion.[13] However, it may still be useful to perform DWI using 3 orthogonal motion-probing gradients in the body to yield both directional and trace DWI images. One clear advantage of calculating the trace image is an improvement in the signal-to-noise ratio by square root of 3 in isotropic regions. In nonisotropic regions (e.g., the kidneys), the trace provides a direction-independent estimate of diffusivity. Review of the directional DWI images can also be helpful when random susceptibility, motion, or EPI artifacts that are present in images of one direction propagate to degrade the trace image.

The use of tetrahedral encoding allows 3 orthogonal motion-probing gradients to be applied simultaneously. Tetrahedral encoding provides the ability to reduce echo-time by combining gradients to obtain high b-values with shorter lengths of MPGs. The reduced echo-time can substantially improve image quality and signal-to-noise and can be used as a strategy to improve the quality of DWI images, but the individual directional images are usually not available for review. Nevertheless, such a technique has been successfully implemented for imaging in the body, including multiple-averaging non-breath-hold DWI.

Reducing artifacts. Diffusion-weighted MR imaging is susceptible to a range of artifacts related to motion, EPI, and susceptibility effects. A detailed account of these is beyond the scope of this article, and the reader is referred to an excellent recent review.[21]

Perhaps, it is worth reflecting upon the nature of motion to which DWI is susceptible. Motion in the body can be thought of as either incoherent or coherent. The former leads to phase dispersion by the motion-probing gradient and results in signal de-

crease at DWI. However, the latter leads only to phase shift and so does not result in significant signal attenuation.

Interestingly, respiratory movement can be viewed as analogous to coherent motion. Muro and colleagues[22] demonstrated this effect in an experiment using fluid-filled phantoms that moved periodically in their long axes along the z-direction of the MR system to simulate respiratory motion. They found that such motion resulted in less than 10% error in ADC measurements of the fluid in the phantom (Fig. 9), and their results suggested that uniform respiratory motion may not lead to significant decrease in DWI signal or substantial errors in ADC measurements, especially over a large nearly uniform structure (e.g., liver). However, respiratory motion can still result in ADC errors in small focal lesions, caused by contamination of signal from adjacent tissues. In addition, movement of the diaphragm at higher speed (or wider excursion) can still lead to blurring of small objects and ADC errors. Bowel peristalsis can also be considered coherent motion (Fig. 10). By contrast, cardiac motion appears to be largely incoherent and can result in severe signal loss in the mediastinum or over the left lobe of the liver (Fig. 11). One technique to minimize such errors and artifacts is to synchronize image acquisition with the source of motion, such as by using cardiac gating and navigator echoes for respiratory triggered acquisitions.

The use of periodically rotated overlapping parallel lines with enhanced reconstruction (PROPELLER) can also help minimize motion effects. PROPELLER is a radial fast spin-echo sequence used with multi-shot imaging. The data is acquired using a series of concentric blades, each of which rotates through the center of the k-space, which reduces any rotation and translation artifacts that occur between the acquisitions of the blades and distributes artifacts uniformly throughout the image.

A major source of artifacts is the eddy currents induced by the rapid switching on and off of the motion-probing gradients, which can lead to geometric distortion as well as image-shearing artifacts that may become more pronounced with increasing

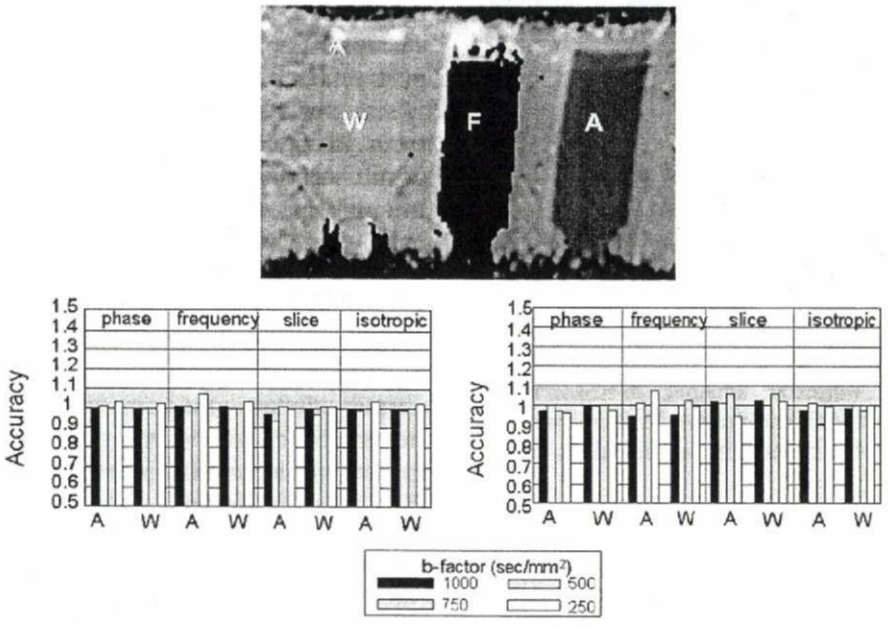

Fig. 9. Effect of motion on apparent diffusion coefficient (ADC) measurements. ADC map of phantoms containing water (W; left), fat (F; middle), and detergent (A; right) embedded in agar. The phantom was scanned moving along the axis of the magnetic resonance scanner simulating respiration. Graphs show the calculated ADC values measured when the phantom was moving at speed of 10 mm/s (lower left) and 20 mm/s (lower right) in the different directions of motion-probing gradients and b-values compared with measurements taken when stationary. Note that the errors for ADC measurement were less than 0.1. This suggests that coherent motion may not affect the ADC measurements. (Permission for reprint obtained by Dr. Takahara from the Nippon Hoshasen Gijutsu Gakkai Zasshi 2005; 61:1551–1558).

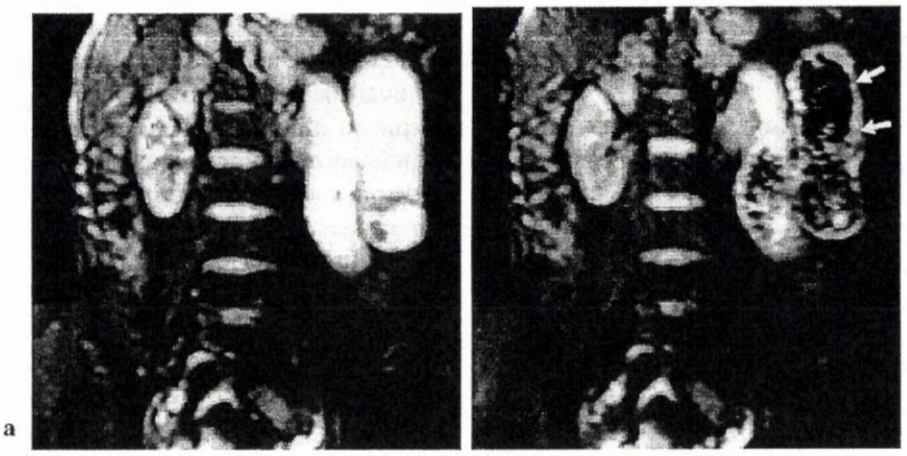

Fig. 10. Small bowel peristalsis. A 52-year-old woman with suspected bowel obstruction. Cine magnetic resonance imaging (not shown) shows good movement in a dilated jejunal loop. Coronal single-shot echo-planar images (**a**) at b $= 0$ s/mm^2 and (**b**) at b $= 50$ s/mm^2 shows that the signal from the jejunal wall (white arrows) is maintained when diffusion weighting is applied in (**b**). However, there is signal attenuation of the luminal contents. This suggests that peristaltic intestinal wall motion is relatively coherent compared with the incoherent motion of luminal turbulence.

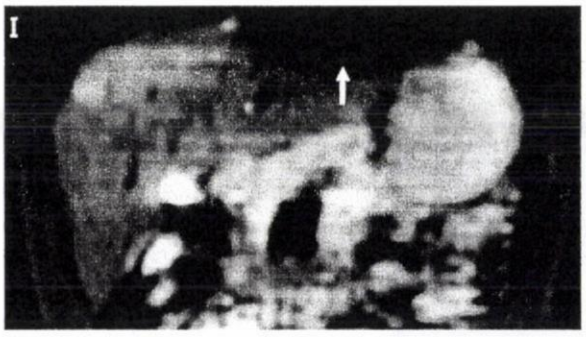

Fig. 11. Signal loss in the left lobe of the liver resulting from cardiac motion. Coronal reformat image of diffusion-weighted imaging (b $= 50$ s/mm^2) shows significant signal attenuation (arrow) over the left lobe of the liver, especially just adjacent to the heart.

b-values. When EPI is employed, there can also be significant magnetization phase shifts that cause "ghosting" artifacts, which are usually worst in the phase-encoding direction. Several adjustments at imaging can help improve image quality, such as changing the band-width, which alters the echo-spacing; and reducing the field of view in the phase encoding direction to a minimum. Increasing the band-width reduces geometric artifacts but can lead to reduction in signal-to-noise and increased ghosting. Because these issues can be complex, it is valuable to engage the expertise of an MR physicist to finely tune the system for optimal performance.

Diffusion-weighted imaging is highly sensitive to susceptibility artifacts. In the abdomen, air in the gastrointestinal tract can cause susceptibility artifacts that obscure visualization of adjacent structures. Intriguingly, it was recently reported that the administration of intravenous Buscopan prior to imaging can worsen the degree of artifacts encountered over the left lobe of the liver.[6]

Quality assurance. To ensure that the MR system is optimized, it is important to develop quality assurance testing as part of the imaging program. One method[23] uses diffusion phantoms made of copper sulphate and sucrose solutions. This allows the precision and accuracy of the ADC measurement to be determined in relation to the noise of the MR imaging system, signal reproducibility, and differences between nominal and effective b-values.[23] In addition, use of these phantoms will allow early recognition of geometric distortion and other eddy current-induced artifacts, thereby enabling their rectification or minimization prior to clinical scanning.

Applications of DWI Techniques for Tumor Assessment

The range of DWI imaging methods described has been employed to assess tumors in the body.[24] Diffusion-weighted imaging has been used to detect[25-28] and characterize[16,29,30] tumors, assess treat-

ment response,[31,32] and provide prognostic information.[33-35] Although not exhaustive, the following account of the clinical applications of DWI illustrates the potential of these techniques.

Breath-hold single shot DWI. Breath-hold single-shot echo planar DWI has been used successfully to evaluate target areas within the abdomen and pelvis. DWI has been applied to detect and characterize tumors in the liver,[18,27,36-40] pancreas,[41] kidneys,[41-45] colon,[46] and prostate.[47,48]

For example, in the liver, breath-hold DWI imaging alone could accurately detect the presence of colorectal hepatic metastases with high sensitivity and specificity[27] (Fig. 12). Application of low diffusion weighting at image acquisition nulls the high signal within intrahepatic blood vessels, thereby facilitating the detection of small metastases lying adjacent to blood vessels. Quantitative ADC measurements can also be calculated using breath-hold DWI, which may aid lesion characterization. It has been shown that malignant hepatic lesions return lower ADC values than do benign lesions, but there is significant overlap.[13] More recently, it was found that high pretreatment ADC values in colorectal hepatic metastases predicted for poor response to chemotherapy.[49] ADC values have also been shown to increase in colorectal hepatic metastases, thus showing at least a partial response to chemotherapy, but not in the nonresponders.[49]

Free-breathing multiple averaging DWI. Free-breathing multiple averaging DWI is a versatile imaging technique that can be applied to virtually any area in the body (Fig. 11). It has been used to evaluate tumors in diverse areas, such as the head and neck,[50,51] pancreas,[25] kidneys,[45,52] and prostate.[53] ADCs can be calculated from the multiple-b-value DWI images acquired, which may help in assessing treatment response.

Diffusion-weighted whole-body imaging with background body signal suppression (DWIBS). Because DWIBS images are usually evaluated qualitatively, the use of just two b-values is usually sufficient ($b = 0$ and 1000 s/mm^2). The choice of a higher b-value in combination with fat suppression results in good background suppression. However, more b-values may be accommodated within the measurement to facilitate the calculation of ADCs.

Initial experience in applying the technique to clinical studies has shown substantial promise. However, DWIBS should be interpreted with other imaging sequences because benign lesions may result in false positives, and certain malignant lesions, such as sclerotic bone metastases, can lead to false negative results. Furthermore, because DWIBS discriminates tissues on the basis of cellularity rather than malignancy, its ability to distinguish between benign and malignant lymph nodes remains uncertain. Its implementation in the evaluation of lymphoma appears promising, but further studies evaluating the clinical applications of the technique are being undertaken. There is also considerable interest in establishing the diagnostic accuracy of the technique in tumor detection compared with whole-body STIR imaging and 18-flurodeoxyglucose positron emission tomography.

Conclusions

Diffusion-weighted MR imaging is useful for assessing tumors. In the body, 3 main DWI strategies are currently applied for tumor imaging. These techniques show considerable promise for detecting

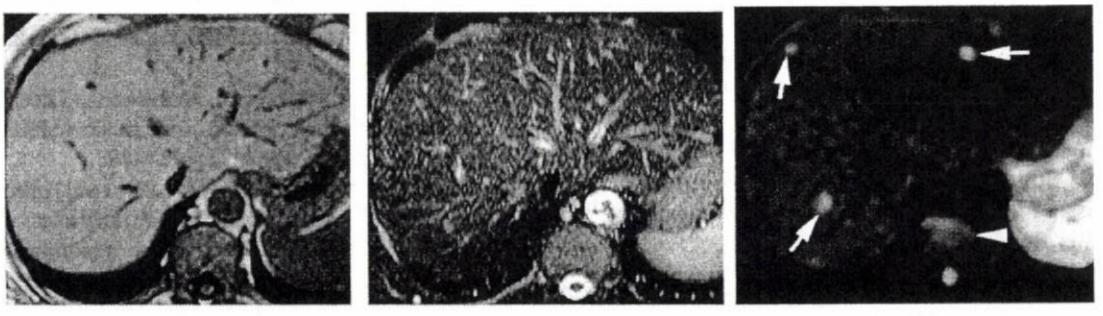

Fig. 12. Lesion detection in the liver using free-breathing diffusion-weighted imaging (DWI). A 45-year-old woman with breast cancer. In this example, metastases were difficult to visualize on the (**a**) unenhanced axial T_1- and (**b**) T_2-weighted images However, at DWI, (**c**) the high signal from intrahepatic vessels is suppressed by application of diffusion gradient on the $b = 100$ s/mm^2 image, enabling the metastases (arrows) to be clearly identified. Note also the incidental finding of a hemangioma within the vertebral body (arrowhead).

and characterizing tumors and evaluating treatment response. However, careful optimization of these techniques is required to ensure high quality images for both qualitative and quantitative assessment. Radiologists should be acquainted with the key factors that affect the quality of DWI studies to ensure effective implementation of these techniques in clinical practice.

References

1. Bammer R. Basic principles of diffusion-weighted imaging. Eur J Radiol 2003; 45:169–184.
2. Yoshikawa T, Kawamitsu H, Mitchell DG, et al. ADC measurement of abdominal organs and lesions using parallel imaging technique. AJR Am J Roentgenol 2006; 187:1521–1530.
3. Oner AY, Celik H, Oktar SO, Tali T. Single breath-hold diffusion-weighted MRI of the liver with parallel imaging: initial experience. Clin Radiol 2006; 61:959–965.
4. Taouli B, Martin AJ, Qayyum A, et al. Parallel imaging and diffusion tensor imaging for diffusion-weighted MRI of the liver: preliminary experience in healthy volunteers. AJR Am J Roentgenol 2004; 183:677–680.
5. Murtz P, Flacke S, Träber F, van den Brink JS, Gieseke J, Schild HH. Abdomen: diffusion-weighted MR imaging with pulse-triggered single-shot sequences. Radiology 2002; 224:258–264.
6. Nasu K, Kuroki Y, Sekiguchi R, Kazama T, Nakajima H. Measurement of the apparent diffusion coefficient in the liver: is it a reliable index for hepatic disease diagnosis? Radiat Med 2006; 24: 438–444.
7. Takahara T, Imai Y, Yamashita T, Yasuda S, Nasu S, Van Cauteren M. Diffusion weighted whole body imaging with background body signal suppression (DWIBS): technical improvement using free breathing, STIR and high resolution 3D display. Radiat Med 2004; 22:275–282.
8. Nasu K, Kuroki Y, Sekiguchi R, Nawano S. The effect of simultaneous use of respiratory triggering in diffusion-weighted imaging of the liver. Magn Reson Med Sci 2006; 5:129–136.
9. Spuentrup E, Buecker A, Koelker C, Guenther RW, Stuber M. Respiratory motion artifact suppression in diffusion-weighted MR imaging of the spine. Eur Radiol 2003; 13:330–336.
10. Takahara T, Yamashita T, Yanagimachi N, Iino M, Koizumi J, Imai Y. Imaging of peripheral nerve disease using diffusion-weighted neurography (DWN) [Abstract SSE13–03], In: Radiological Society of North America Scientific Assembly and Annual Meeting. Chicago, 2004; 394.
11. Farraher SW, Jara H, Chang KJ, Ozonoff A, Soto JA. Differentiation of hepatocellular carcinoma and hepatic metastasis from cysts and hemangiomas with calculated T_2 relaxation times and the T_1/T_2 relaxation times ratio. J Magn Reson Imaging 2006; 24:1333–1341.
12. Provenzale JM, Engelter ST, Petrella JR, Smith JS, MacFall JR. Use of MR exponential diffusion-weighted images to eradicate T_2 "shine-through" effect. AJR Am J Roentgenol 1999; 172:537–539.
13. Taouli B, Vilgrain V, Dumont E, Daire JL, Fan B, Menu Y. Evaluation of liver diffusion isotropy and characterization of focal hepatic lesions with two single-shot echo-planar MR imaging sequences: prospective study in 66 patients. Radiology 2003; 226:71–78.
14. Ichikawa T, Haradome H, Hachiya J, Nitatori T, Araki T. Diffusion-weighted MR imaging with a single-shot echoplanar sequence: detection and characterization of focal hepatic lesions. AJR Am J Roentgenol 1998; 170:397–402.
15. Müller MF, Prasad PV, Siewert B, Edelman RR. [The *in-vivo* diffusion measurements of the liver, kidneys, spleen and m. erector with an echo-planar imaging system in normal subjects]. Rofo 1994; 161:233–236. (Article in German)
16. Namimoto T, Yamashita Y, Sumi S, Tang Y, Takahashi M. Focal liver masses: characterization with diffusion-weighted echo-planar MR imaging. Radiology 1997; 204:739–744.
17. Yamada I, Aung W, Himeno Y, Nakagawa T, Shibuya H. Diffusion coefficients in abdominal organs and hepatic lesions: evaluation with intravoxel incoherent motion echo-planar MR imaging. Radiology 1999; 210:617–623.
18. Koh DM, Scurr E, Collins DJ, et al. Colorectal hepatic metastases: quantitative measurements using single-shot echo-planar diffusion-weighted MR imaging. Eur Radiol 2006; 16:1898–1905.
19. Hollingsworth KG, Lomas DJ. Influence of perfusion on hepatic MR diffusion measurement. NMR Biomed 2006; 19:231–235.
20. Moteki T, Horikoshi H. Evaluation of hepatic lesions and hepatic parenchyma using diffusion-weighted echo-planar MR with three values of gradient b-factor. J Magn Reson Imaging 2006; 24:637–645.
21. Le Bihan D, Poupon C, Amadon A, Lethimonnier F. Artifacts and pitfalls in diffusion MRI. J Magn Reson Imaging 2006; 24:478–488.
22. Muro I, Takahara T, Horie T, et al. [Influence of respiratory motion in body diffusion weighted imaging under free breathing (examination of a moving phantom)]. Nippon Hoshasen Gijutsu Gakkai Zasshi 2005; 61:1551–1558. (Article in Japanese)
23. Delakis I, Moore EM, Leach MO, De Wilde JP. Developing a quality control protocol for diffusion imaging on a clinical MRI system. Phys Med Biol 2004; 49:1409–1422.
24. Koh DM, Collins DJ. Diffusion-weighted MRI in the body: applications and challenges in oncology.

AJR Am J Roentgenol 2007; 188:1622–1635.
25. Ichikawa T, Erturk SM, Motosugi U, et al. High-b value diffusion-weighted MRI for detecting pancreatic adenocarcinoma: preliminary results. AJR Am J Roentgenol 2007; 188:409–414.
26. Ichikawa T, Erturk SM, Motosugi U, et al. High-B-value diffusion-weighted MRI in colorectal cancer. AJR Am J Roentgenol 2006; 187:181–184.
27. Nasu K, Kuroki Y, Nawano S, et al. Hepatic metastases: diffusion-weighted sensitivity-encoding versus SPIO-enhanced MR imaging. Radiology 2006; 239:122–130.
28. Naganawa S, Sato C, Nakamura T, et al. Diffusion-weighted images of the liver: comparison of tumor detection before and after contrast enhancement with superparamagnetic iron oxide. J Magn Reson Imaging 2005; 21:836–840.
29. Chan JH, Tsui EY, Luk SH, et al. Diffusion-weighted MR imaging of the liver: distinguishing hepatic abscess from cystic or necrotic tumor. Abdom Imaging 2001; 26:161–165.
30. Kim T, Murakami T, Takahashi S, Hori M, Tsuda K, Nakamura H. Diffusion-weighted single-shot echoplanar MR imaging for liver disease. AJR Am J Roentgenol 1999; 173:393–398.
31. Byun WM, Shin SO, Chang Y, Lee SJ, Finsterbusch J, Frahm J. Diffusion-weighted MR imaging of metastatic disease of the spine: assessment of response to therapy. AJNR Am J Neuroradiol 2002; 23:906–912.
32. Chen CY, Li CW, Kuo YT, et al. Early response of hepatocellular carcinoma to transcatheter arterial chemoembolization: choline levels and MR diffusion constants–initial experience. Radiology 2006; 239:448–456.
33. Mardor Y, Roth Y, Ochershvilli A, et al. Pretreatment prediction of brain tumors' response to radiation therapy using high b-value diffusion-weighted MRI. Neoplasia 2004; 6:136–142.
34. Dzik-Jurasz A, Domenig C, George M, et al. Diffusion MRI for prediction of response of rectal cancer to chemoradiation. Lancet 2002; 360:307–308.
35. Provenzale JM, Mukundan S, Barboriak DP. Diffusion-weighted and perfusion MR imaging for brain tumor characterization and assessment of treatment response. Radiology 2006; 239:632–649.
36. Okada Y, Ohtomo K, Kiryu S, Sasaki Y. Breath-hold T_2-weighted MRI of hepatic tumors: value of echo planar imaging with diffusion-sensitizing gradient. J Comput Assist Tomogr 1998; 22:364–371.
37. Abe Y, Yamashita Y, Tang Y, Namimoto T, Takahashi M. Calculation of T_2 relaxation time from ultrafast single shot sequences for differentiation of liver tumors: comparison of echo-planar, HASTE, and spin-echo sequences. Radiat Med 2000; 18:7–14.
38. Yamashita Y, Tang Y, Takahashi M. Ultrafast MR imaging of the abdomen: echo planar imaging and diffusion-weighted imaging. J Magn Reson Imaging 1998; 8:367–374.
39. Ito K, Mitchell DG, Matsunaga N. MR imaging of the liver: techniques and clinical applications. Eur J Radiol 1999; 32:2–14.
40. Quan XY, Sun XJ, Yu ZJ, Tang M. Evaluation of diffusion weighted imaging of magnetic resonance imaging in small focal hepatic lesions: a quantitative study in 56 cases. Hepatobiliary Pancreat Dis Int 2005; 4:406–409.
41. Chow LC, Bammer R, Moseley ME, Sommer FG. Single breath-hold diffusion-weighted imaging of the abdomen. J Magn Reson Imaging 2003; 18: 377–382.
42. Squillaci E, Manenti G, Di Stefano F, Miano R, Strigari L, Simonetti G. Diffusion-weighted MR imaging in the evaluation of renal tumours. J Exp Clin Cancer Res 2004; 23:39–45.
43. Squillaci E, Manenti G, Cova M, et al. Correlation of diffusion-weighted MR imaging with cellularity of renal tumours. Anticancer Res 2004; 24:4175–4179.
44. Cova M, Squillaci E, Stacul F, et al. Diffusion-weighted MRI in the evaluation of renal lesions: preliminary results. Br J Radiol 2004; 77:851–857.
45. Pozzi-Mucelli R. Can diffusion-weighted MRI without breath-holding be used to evaluate renal abnormalities? Nat Clin Pract Nephrol 2006; 2:126–127.
46. Nasu K, Kuroki Y, Kuroki S, Murakami K, Nawano S, Moriyama N. Diffusion-weighted single shot echo planar imaging of colorectal cancer using a sensitivity-encoding technique. Jpn J Clin Oncol 2004; 34:620–626.
47. Hosseinzadeh K, Schwarz SD. Endorectal diffusion-weighted imaging in prostate cancer to differentiate malignant and benign peripheral zone tissue. J Magn Reson Imaging 2004; 20:654–661.
48. Reinsberg SA, Payne GS, Riches SF, et al. Combined use of diffusion-weighted MRI and ^{1}H MR spectroscopy to increase accuracy in prostate cancer detection. AJR Am J Roentgenol 2007; 188:91–98.
49. Koh DM, Scurr E, Collins DJ, et al. Predicting response of colorectal hepatic metastases: value of pre-treatment apparent diffusion coefficients. AJR Am J Roentgenol 2007; 188:1001–1008
50. Koç O, Paksoy Y, Erayman I, Kivrak AS, Arbag H. Role of diffusion weighted MR in the discrimination diagnosis of the cystic and/or necrotic head and neck lesions. Eur J Radiol 2007; 62:205–213.
51. Vandecaveye V, De Keyzer F, Nuyts S, et al. Detection of head and neck squamous cell carcinoma with diffusion weighted mri after (chemo) radiotherapy: Correlation between radiologic and histopathologic findings. Int J Radiat Oncol Biol Phys 2007; 67:960–971.
52. Thoeny HC, De Keyzer F, Oyen RH, Peeters RR.

Diffusion-weighted MR imaging of kidneys in healthy volunteers and patients with parenchymal diseases: initial experience. Radiology 2005; 235: 911–917.

53. Kurhanewicz J, Vigneron DB, Males RG, Swanson MG, Yu KK, Hricak H. The prostate: MR imaging and spectroscopy. Present and future. Radiol Clin North Am 2000; 38:115–138, viii-ix.

Jpn J Clin Oncol 2008;38(8)534–539
doi:10.1093/jjco/hyn072

Trends in Lung Cancer Incidence by Histological Type in Osaka, Japan

Yasuhiro Toyoda[1,2], Tomio Nakayama[1], Akiko Ioka[1] and Hideaki Tsukuma[1]

[1]Department of Cancer Control and Statistics, Osaka Medical Center for Cancer and Cardiovascular Disease, and [2]Public Health, Department of Social and Environmental Medicine, Graduate School of Medicine, Osaka University, Osaka, Japan

Received March 11, 2008; accepted July 13, 2008; published online August 9, 2008

Background: In Japan, an increase in age-adjusted incidence rates of lung adenocarcinoma (ADC) and a decrease in lung squamous cell carcinoma (SQCC) have been reported.
Methods: The number of lung cancer incidence, age-adjusted rates, and age-specific rates by birth-cohort according to histological type were examined using the data from Osaka Cancer Registry.
Results: The numbers of lung cancer incidence among men and women have increased, particularly in ADC. The age-adjusted incidence rates of ADC among men and women have continuously increased, while those of SQCC and small cell carcinoma (SMCC) turned to decrease since 1990s. A trough of lung cancer incidence rates was observed among men in 1935–39 birth-cohorts. The declining trend appeared in 1955–59 birth-cohorts. Lung cancer incidence rates among women have increased since 1895–99 birth-cohorts, but those rates leveled off or decreased in 1950s birth-cohorts. Trends of ADC by birth-cohort were almost the same as those of all histological types. The SQCC among men peaked in 1915–19 birth-cohorts, and decreased in the subsequent birth-cohorts. The SMCC among men peaked in 1920s birth-cohorts, and decreased or leveled off in the subsequent birth-cohorts.
Conclusions: Lung cancer incidence rates by birth-cohorts were almost parallel to the smoking prevalence. However, those for ADC among young women in 1950s birth-cohorts were not parallel to the smoking prevalence, which requires careful monitoring to confirm such findings.

Key words: lung cancer – incidence – histological type – birth-cohort

BACKGROUND

Lung cancer is the leading cause of cancer deaths in Japan, with 45 927 men and 17 307 women dying from lung cancer in 2006. To date, increase in the incidence rates of lung adenocarcinoma (ADC) and decrease in the incidence rates of squamous cell carcinoma (SQCC) and small cell carcinoma (SMCC) have been reported in Japan (1,2). The same trend has been reported in Western countries also (3–5). Some previous studies reported that there was a trough of lung cancer incidence or mortality in Japanese male 1935–39 birth-cohorts because of the limited cigarette supply just after World War II (6–10). Soda et al. (7) reported the birth-cohort analysis by histological type using Nagasaki Cancer Registry in 2000. However, this study was based on the small number of registered lung cancer cases and excluded the cases without histological diagnoses.

In the present study, we updated the recent trends in lung cancer incidence by histological type and tried to clarify their characteristics by birth-cohort, using the data from Osaka Cancer Registry (OCR) with the large number of lung cancer incidence.

MATERIALS AND METHODS

OCR, which started in 1962, is the population-based cancer registry covering Osaka prefecture (population: 8.8 million, 2005 census). Using OCR data on lung cancer incidence

For reprints and all correspondence: Tomio Nakayama, Department of Cancer Control and Statistics, Osaka Medical Center for Cancer and Cardiovascular Disease, 537-8511 3-3 Nakamichi 1-chome, Higashinari-ku, Osaka 537-8511, Japan. E-mail: nakayama-to@mc.pref.osaka.jp

(International Classification of Diseases 10th revision C33–C34) diagnosed between 1975 and 2003, we calculated the number of lung cancer incidence per year, age-adjusted rates and age-specific rates by birth-cohort according to histological type.

Histological types were categorized into three major types: ADC (ICD-O: 8140, 8141, 8200, 8211, 8250, 8251, 8260, 8310, 8323, 8440, 8470, 8480, 8481 and 8490), SQCC (ICD-O: 8050, 8052 and 8070–8076), SMCC (ICD-O: 8041–8045) and the others.

Incident years are divided into 5-year periods: 1975–78, 1979–83, 1989–93, 1994–98 and 1999–2003. Birth years were also divided into 5-year periods. The population data by age group in Osaka prefecture were obtained from the data of Population Census. For age-standardization, the Japanese model population in 1985 was used.

The data from OCR included the cases without specific histological diagnosis: a maximum of 60.4% in 1975–78 and a minimum of 31.4% in 1994–98. Based on the assumption that distributions of histological types in the same sex and age group were the same between those with and without a specific histological type, we compensated for the proportion of cases without a specific histological type. The detailed procedure was followed to the previous study (1); first, the sex-, age (5-year)- and incident year (or birth-cohort)-specific numbers of incidence were calculated for all histological types including the cases without histological diagnosis. Second, the sex-, age (10-year)- and incident year (or birth-cohort)-specific proportion of each histological type among the cases with histological diagnosis were calculated for three major histological types. Finally, the sex-, age (5-year)-, incident year (or birth-cohort)-specific number of incidence were multiplied by the corresponding sex-, age- and incident year (or birth-cohort)-specific proportion to approximate the number of incidence by histological type.

RESULTS

Table 1 shows the trends in the number of lung cancer incidence per year according to histological type. Lung cancer incidence per year for all histological types among men and women increased consistently; from 1086 in 1975–78 to 3487 in 1999–2003 among men and from 395 in 1975–78 to 1482 in 1999–2003 among women. As for histological type, the number of ADC incidence has increased remarkably among men and women. The shift in main histological type among men occurred in the 1990s.

Table 2 shows the trends in the age-adjusted rates according to the histological type. The age-adjusted rates for all histological types peaked in 1994–98 and recently leveled off among men, while those consistently increased among women. The rates for ADC consistently increased among men and women. In contrast, the rates for SQCC and SMCC peaked in 1989–93 among men, and decreased subsequently. Those rates for SQCC and SMCC peaked in 1984–88 and 1989–93, respectively, among women, and decreased subsequently.

Fig. 1 shows the trends in the age-specific lung cancer incidence rates with 95% confidence interval by birth-cohort for all histological types. Among men, there was a trough in rates for all age groups in 1935–39 birth-cohorts, which was consistent with the previous findings (7,10). In the subsequent birth-cohorts, the rates increased for all age groups, but the declining tendency appeared in 1955–59 birth-cohorts. Among women, the trough in rates in 1935–39 birth-cohorts was not confirmed. The rates for aged ≥ 50 years increased gradually, while it seemed that the rates for aged < 50 years turned to decrease or level off after 1950–54 birth-cohorts: however, these trends were unstable because of the wide confidence intervals due to the small number of incidence.

Table 1. Trends in the number of lung cancer incidence per year according to histological type

Histological type	Incident year					
	1975–78	1979–83	1984–88	1989–93	1994–98	1999–2003
Men						
Adenocarcinoma (%)	372 (34.2)	510 (35.7)	696 (35.5)	853 (35.8)	1191 (40.2)	1497 (42.9)
Squamous cell carcinoma (%)	474 (43.6)	582 (40.8)	760 (38.8)	921 (38.6)	1086 (36.6)	1208 (34.7)
Small cell carcinoma (%)	142 (13.0)	203 (14.2)	315 (16.1)	410 (17.2)	483 (16.3)	543 (15.6)
Others (%)	99 (9.1)	132 (9.3)	189 (9.7)	200 (8.4)	204 (6.9)	239 (6.8)
All histological types (%)	1086 (100)	1428 (100)	1961 (100)	2383 (100)	2964 (100)	3487 (100)
Women						
Adenocarcinoma (%)	242 (61.2)	328 (60.2)	453 (58.7)	579 (60.3)	792 (64.8)	996 (67.2)
Squamous cell carcinoma (%)	86 (21.9)	106 (19.5)	163 (21.2)	184 (19.2)	218 (17.9)	241 (16.3)
Small cell carcinoma (%)	32 (8.0)	73 (13.3)	97 (12.5)	132 (13.7)	152 (12.5)	178 (12.0)
Others (%)	35 (8.9)	38 (6.9)	59 (7.5)	65 (6.8)	60 (4.9)	66 (4.4)
All histological types (%)	395 (100)	545 (100)	772 (100)	961 (100)	1223 (100)	1482 (100)

Table 2. Trends in age-adjusted lung cancer incidence rates per 100 000 person-years according to histological type

Histological type	Incident year					
	1975–78	1979–83	1984–88	1989–93	1994–98	1999–2003
Men						
Adenocarcinoma	15.5	18.9	21.7	22.3	26.0	27.2
Squamous cell carcinoma	20.4	22.2	25.0	25.6	24.8	22.3
Small cell carcinoma	6.0	7.6	10.1	11.1	10.8	10.0
All histological types	46.2	53.7	62.9	64.7	66.5	64.3
Women						
Adenocarcinoma	7.9	9.2	10.5	11.3	13.1	13.8
Squamous cell carcinoma	2.8	3.0	3.8	3.5	3.4	3.1
Small cell carcinoma	1.0	2.0	2.3	2.5	2.4	2.3
All histological types	12.9	15.2	17.9	18.6	19.9	20.2

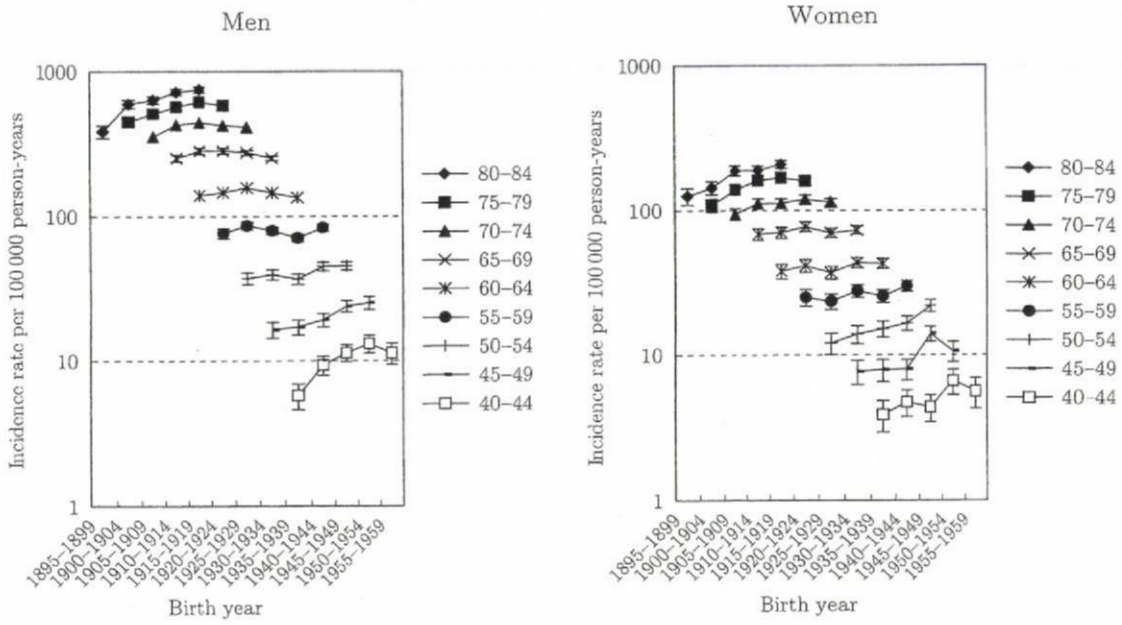

Figure 1. Trends in age-group-specific lung cancer incidence rates with 95% confidence interval by birth-cohort for all histological types.

Figs 2–4 show the trends in the age-specific incidence rates with 95% confidence interval by birth-cohort for ADC, SQCC and SMCC, respectively. The rates for ADC among men increased gradually for all age groups, but the declining tendency appeared in 1955–59 birth-cohorts. Furthermore, it seemed that there was a slight trough in rates in 1935–39 birth-cohorts, as well as findings in all histological types. The trends in ADC among women were almost similar with those in all histological types. The rates for SQCC among men peaked in 1910–14 birth-cohorts and decreased in the subsequent birth-cohorts. The trough in rates during 1935–39 birth-cohorts was not clear for SQCC among men. Trends in the rates for SQCC among women aged ≥65 years were similar with those among men. The trends in aged <65 years were, however, unclear because of the wide confidence interval. The rates for SMCC among men peaked around 1920s birth-cohorts and turned to slightly decrease or level off in the subsequent birth-cohorts. The rates for SMCC among women were unclear because of the wide confidence interval.

DISCUSSION

In the present study, we reported the population-based trends in lung cancer incidence including birth-cohort analyses according to histological type using OCR. The number of lung cancer incidence per year increased continuously because of the population aging. The main histological type of lung cancer switched from SQCC to ADC among men in

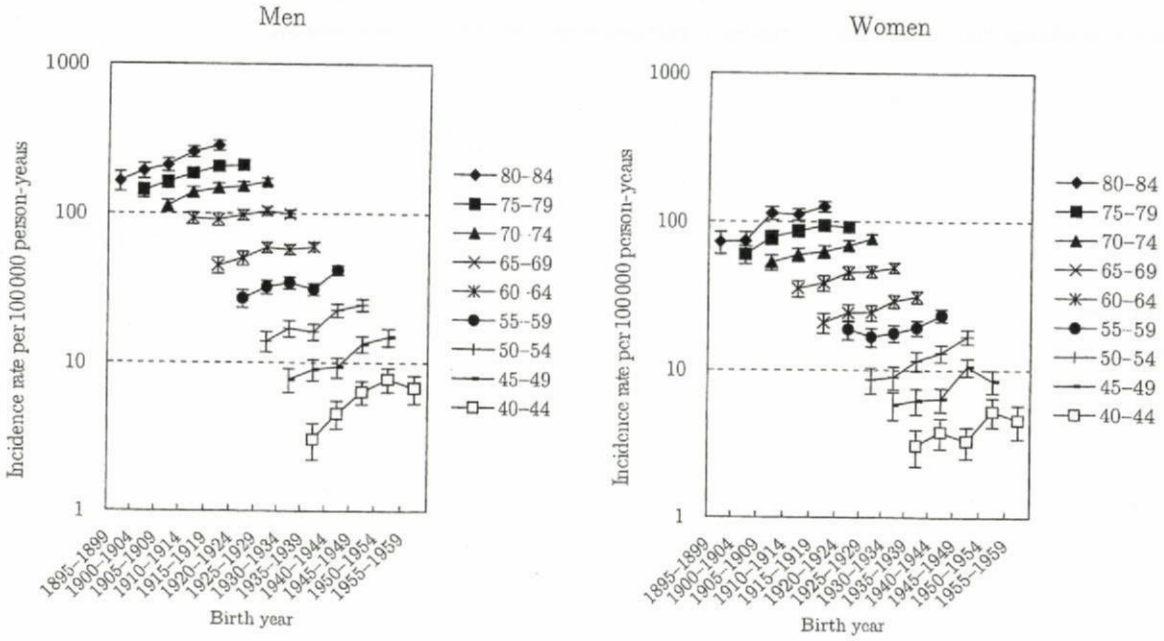

Figure 2. Trends in age-group-specific incidence rates with 95% confidence interval by birth-cohort for adenocarcinoma.

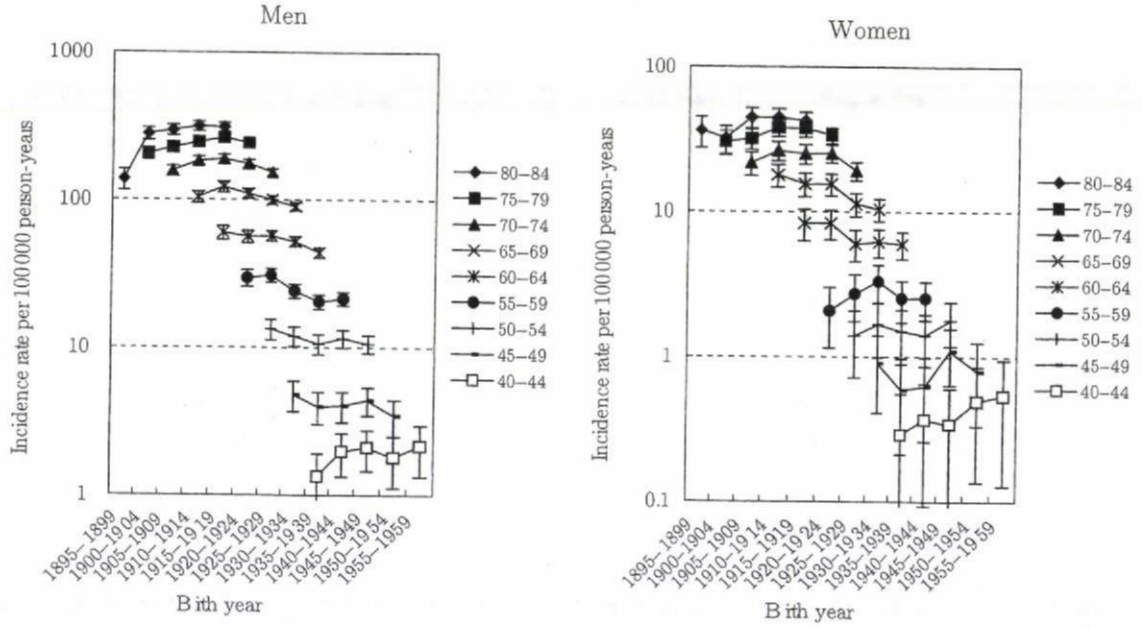

Figure 3. Trends in age-group-specific incidence rates with 95% confidence interval by birth-cohort for squamous cell carcinoma.

1990s. The declining trends for SQCC and SMCC continued in the updated present study.

Smoking prevalence by birth-cohort among Japanese men was reported to have two peaks: around the 1925 birth-cohort and around the 1950 birth-cohort (11). In addition, there was a trough of smoking prevalence in 1930–40 birth-cohorts because of the limited cigarette supply just after World War II (11). In general, the trends in lung cancer incidence or mortality by birth-cohort were parallel to the trends in the smoking prevalence. Our results were consistent with the findings from previous studies, showing that lung cancer mortality and incidence rates among men in 1935–39 birth-cohorts were lower than the subsequent birth-cohorts (6–10). Since the smoking prevalence among Japanese men was declining after 1950s birth-cohorts, the appearance of declining trends of lung cancer incidence among men in 1955–59 birth-cohorts was an expected result.

Classically, smoking behavior was considered to be more strongly associated with SQCC than with ADC. However, SQCC incidence rates by birth-cohort among men were not

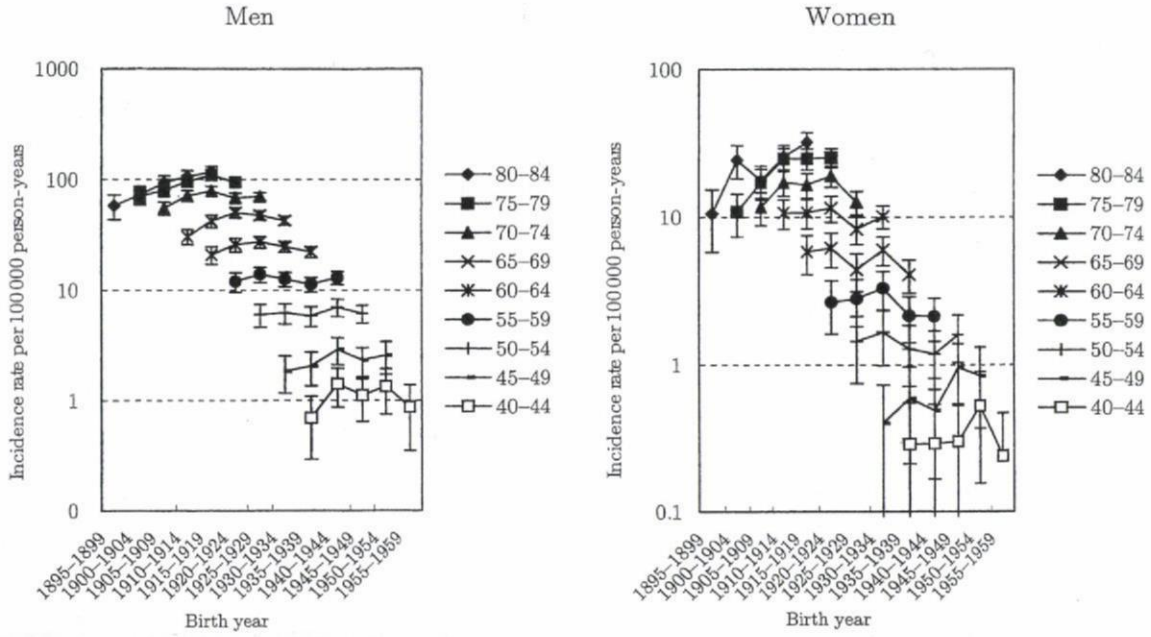

Figure 4. Trends in age-group-specific incidence rates with 95% confidence interval by birth-cohort for small cell carcinoma.

parallel to the smoking prevalence by birth-cohort. SQCC incidence rates among men after 1940–44 birth-cohorts leveled off, whereas the smoking prevalence among men after 1940–44 birth-cohorts increased. One reason would be the switching from non-filtered cigarettes to filtered cigarettes. Filtered cigarettes were considered to be associated with peripheral ADC because of the deep inhalation (3,12,13). According to the information from Japan Tobacco Inc., the switching from non-filtered cigarettes to filtered cigarettes occurred in the 1960s in Japan (14). The shift from SQCC to ADC among men in 1990s observed in the present study might have been the result of this shift in cigarette types.

The smoking prevalence by birth-cohort among women is continuously increasing after 1930s birth-cohorts (11). However, lung cancer incidence among women in 1950s birth-cohorts, particularly for ADC, seemed to be leveling off or decreasing. Marugame et al. (15) also reported the trends in lung cancer mortality by birth-cohort using the National Vital Statistics. In that study, lung cancer mortality trends appeared to be decreasing for female birth-cohorts born after 1960. Although our results were unstable because of the wide confidence intervals, those were not contradictory to this previous study. There is no clear explanation for these findings among younger Japanese women. There would be some factors other than active smoking for lung cancer incidence among them.

The present study has some limitations. First, there may be some missing cases in the OCR. The proportion of death certificate only for lung cancer in OCR was 19.3% in 1998–2002 (16). Therefore, lung cancer incidence may be under-estimated as a whole. Secondly, the trends by histological type among young women were unstable because of the small number of incidence; the number of lung cancer incidence among women aged <50 years per year was ~80 cases in 2003. Finally, the data from OCR included many lung cancer cases without specific histological diagnoses. We had to use assumption in order to calculate the number of incidence according to histological type. The proportions of lung cancer cases without histological diagnoses for aged <80 years decreased between 1975–78 and 1999–2003; from 49.7 to 16.4% among aged 40–49 years, from 47.4 to 17.6% among aged 50–59 years, from 55.9 to 22.7% among aged 60–69 years and from 70.8 to 31.6% among aged 70–79 years, respectively. However, those for aged ≥80 years were still high: from 78.9 to 64.1%. Therefore, we require carefulness to interpret the findings, particularly for elderly.

In conclusion, we reported recent trends in lung cancer incidence according to histological type. The increase in ADC incidence and the decrease in SQCC and SMCC incidence were confirmed. The trends in lung cancer incidence among young women in 1950s birth-cohorts, particularly for ADC, were not parallel to the smoking prevalence. We need careful monitoring of the trends in lung cancer incidence, particularly for ADC among young women.

Acknowledgements

We would like to thank Dr Akira Oshima, Cancer Patients Information Service, Osaka Medical Center for Cancer and Cardiovascular Disease, and Professor Hiroyasu Iso, Public Health, Department of Social and Environmental Medicine, Osaka University Graduate School of Medicine for their valuable comments. We also thank the staff at the Osaka Cancer Registry for data collection.